Anisotropy of infrared-active phonon modes in the monodomain state of tetragonal SrTiO₃ (110)

M. Yazdi-Rizi,[*] P. Marsik, B. P. P. Mallett, and C. Bernhard[†]

Department of Physics and Fribourg Center for Nanomaterials, University of Fribourg, Chemin du Musée 3, CH-1700 Fribourg, Switzerland

With infrared (IR) and terahertz (THz) ellipsometry we investigated the anisotropy of the IR-active phonon modes in SrTiO₃ (110) single crystals in the tetragonal state below the so-called antiferrodistortive transition at $T^* = 105$ K. In particular, we show that the anisotropy of the oscillator strength of the so-called R mode, which becomes weakly IR active below T^*, is a valuable indicator of the orientation of the structural domains. Our results reveal that a monodomain state with the tetragonal axis (c axis) parallel to the [001] direction can be created by applying a moderate uniaxial stress of about 2.3 MPa along the [1-10] direction (with a simple mechanical clamp). The resulting splitting of the IR-active phonon modes is reported.

I. INTRODUCTION

SrTiO₃ (STO) is widely used as a substrate for growing thin films and multilayers of various complex oxides. Furthermore, the interface of STO with other insulating oxide perovskites, like LaAlO₃ (LAO), has become a subject of great interest since it was found that it can host a two-dimensional electron gas with a very high mobility [1,2] and even superconductivity [3] at low temperature and ferromagnetism [4]. These developments have renewed the interest in the structural and electronic properties of bulk STO.

With decreasing temperature, STO undergoes a series of structural phase transitions which break several symmetries [5]. The first, the so-called anitferrodistortive transition at $T^* = 105$ K from a cubic to a tetragonal symmetry, involves an antiphase rotation of the neighboring TiO₆ octahedra around the c axis, as shown in Fig. 1(a). It gives rise to a doubling of the unit cell along all three directions and a slightly larger lattice parameter in the direction of the rotation axis (c axis) compared to the perpendicular ones (a axis), with a ratio of $c/a \approx 1.0015$ at low temperature [6]. There are further structural transitions into an orthorhombic state around 65 K and a rhombohedral one at 37 K [7]. Below about 25 K STO enters a so-called incipient ferroelectric or quantum paraelectric state [8], for which a ferroelectric order is prohibited only by the ionic quantum fluctuations [9]. Finally, at $T < 10$ K it has been reported that STO can exhibit a piezoelectric response [10].

The structural and electronic properties of STO are rather sensitive to strain and defects. In the tetragonal state below $T^* = 105$ K this typically results in a structural polydomain state with different orientations of the tetragonal axis (c axis) [11,12]. These polydomain structures and their microscopic imprint on the physical properties of STO and heterostructures in which STO serves as a substrate are well documented [13–15]. A preferred orientation of these structural domains can be achieved by applying uniaxial pressure [16,17] or large electric fields [18]. Furthermore, it was shown that the direction of the surface cut of the STO crystals can strongly affect the orientation of these structural domains. Whereas

STO crystals with a (001) surface are typically in a highly twinned polydomain state, the STO crystals with a (110) surface have a strong tendency for a monodomain state for which the tetragonal axis is along the [001] direction [17,19]. The latter may well be related to the anisotropy of the (110) surface [20,21]. Furthermore, the surface of STO (110) is polar and thus tends to undergo a reconstruction [22–24].

An important role of the surface in the antiferrodistortive transition is also suggested by the finding that in the vicinity of the sample surface this transition can occur at considerably higher temperatures (with $T^* \leqslant 150$ K) than in the bulk (with $T^* = 105$ K). The details have been shown to strongly depend on the residual strain that arises from the surface preparation, e.g., by lapping, grinding, or cutting [25] or the strain due to a thin film on top of the STO substrate [6]. This raises the question of whether in thick STO (110) single crystals the domain alignment is limited to the near-surface region [25] or also occurs in the bulk.

In the following we use the anisotropy of the IR-active phonon modes, in particular, of the so-called R mode, which becomes IR active below $T^* = 105$ K, to study the structural domain formation in STO (110) crystals with a thickness of up to 1 mm. We find that the pristine STO (110) crystals are already partially detwinned with the tetragonal axis oriented along the [001] direction. Furthermore, we show that a relatively small uniaxial stress of 2.3 MPa is already sufficient to obtain a true monodomain state. Notably, we found that this monodomain state was almost persevered after the samples had been warmed to room temperature and cooled again without the unidirectional stress. Finally, we have also determined the anisotropy of the other three IR-active phonon modes, which is rather weak and in agreement with the small anisotropy ratio of $c/a \approx 1.0015$ [6].

II. EXPERIMENTAL DETAILS

The IR ellipsometry measurements have been performed with a home-built setup that is equipped with a He flow cryostat and attached to a Bruker 113V fast Fourier spectrometer as described in Ref. [26]. The data have been taken at different temperatures in the rotating analyzer mode, with and without a static compensator based on a ZnSe prism. The terahertz (THz) optical response has been measured with a home-built

---

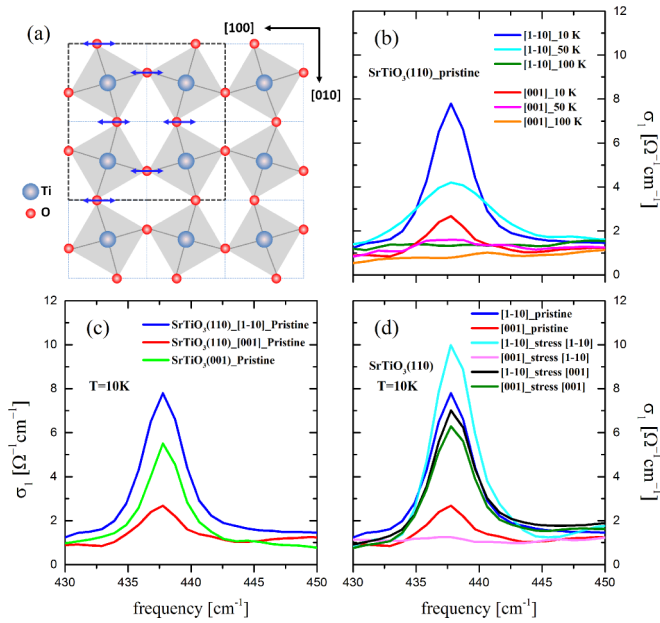[*]meghdad.yazdi@unifr.ch
[†]christian.bernhard@unifr.ch

FIG. 1. (a) Sketch of the tetragonal structure of STO below $T^* = 105$ K with the antiphase rotation of the TiO$_6$ octahedra around the tetragonal axis (c axis). (b) Spectra of the real part of the optical conductivity of pristine STO (110) showing the so-called R-mode along the [1-10] and [001] directions at different temperatures below $T^* = 105$ K. (c) Comparison of the R mode at $T = 10$ K in pristine STO (001) and STO (110) crystals that are lightly and heavily twinned, respectively. (d) The effect of a uniaxial stress of 2.3 MPa applied along the [1-10] and [001] directions on the spectra of the R mode along [1-10] and [001], respectively.

time-domain THz ellipsometer that is described in Ref. [27]. For both ellipsometers the angle of incidence of the light was set to 75°.

For anisotropic samples the ellipsometric measurements are predominantly sensitive to the response along the plane of incidence of the reflected light [28]. Accordingly, for the present STO (110) crystals, which in the tetragonal state exhibit a uniaxial anisotropy with the [001] symmetry axis parallel to the surface, we measured the dielectric response functions along the [001] and [1-10] directions by rotating the sample by appropriate angles around the surface normal. The optical conductivity data for the two orientations as shown in this paper have been obtained by directly calculating the pseudodielectric function $\langle \varepsilon \rangle$ from the measured ellipsometric angles Ψ and Δ, where $r_p/r_s = \tan(\Psi)e^{i\Delta}$ and r_p and r_s are the Fresnel reflection coefficients for p- and s-polarized light. During all the optical measurements special care was taken to avoid photodoping effects by shielding the sample against visible and UV light [29]. To apply a uniaxial stress of about 2.3 MPa, along either the [001] or the [1-10] direction, we mounted the sample in a spring-loaded clamp and cooled it slowly to low temperature. For the stress-free measurements the sample was glued with silver paint to a different sample holder. The STO (110) single crystals were purchased from SurfaceNet and had dimensions of $10 \times 10 \times 1$ mm^3, $10 \times 10 \times 0.5$ mm^3, $5 \times 5 \times 1$ mm^3, and $5 \times 5 \times 1$ mm^3, respectively.

III. EXPERIMENTAL RESULTS

In the cubic state at $T > T^*$ STO has three IR-active transversal-optical (TO) phonon modes that are triply degenerate [30,31]. At the lowest frequency is the so-called soft mode (or Slater mode) with an eigenfrequency of $\omega_0 \approx 95$ cm^{-1} at 300 K which decreases to about 15 cm^{-1} at 10 K. It involves the displacement of the Ti ion against the surrounding oxygen octahedron and is at the heart of the quantum paraelectric behavior of STO. The phonon at 170 cm^{-1} is the so-called external mode (or Last mode) due to the displacement of the Sr ions against the TiO$_6$ octahedron. At the highest energy of about 545 cm^{-1} is the so-called stretching mode (or Axe mode), which stretches the oxygen octahedra.

In the tetragonal state below $T^* = 105$ K an additional mode becomes weakly IR active due to the antiphase rotation of the neighboring oxygen octahedra, as sketched in Fig. 1(a). It is the so-called R mode at 438 cm^{-1} [7] that arises from the doubling of the unit cell and the subsequent back-folding of the phonon modes from the boundary (the R point) to the center of the Brillouin zone [11,32]. The oscillator strength of this R mode is proportional to the magnitude of the antiphase rotation of the TiO$_6$ octahedra. Furthermore, its strength exhibits a characteristic dependence on the polarization direction of the IR light with respect to the tetragonal axis. It is maximal if the polarization is perpendicular to the rotation axis of the oxygen octahedra (to the tetragonal axis), and it vanishes when it is parallel. The large sensitivity of the R mode to such structural changes has already been demonstrated in Ref. [33].

In the following we show that this anisotropy of the oscillator strength of the R mode can be used to determine the orientation of the tetragonal axis in STO single crystals and its variation in a structural multidomain state. Figure 1(b) shows the temperature and polarization dependence of the R mode of a pristine STO (110) single crystal in terms of the real part of the optical conductivity. It confirms that the oscillator strength of the R mode is strongly anisotropic; that is, it is almost four times larger along the [1-10] direction than along [001]. Figure 1(c) shows a comparison of the R modes in pristine STO (110) and STO (001) single crystals. For the latter the oscillator strength is isotropic [this has been confirmed for several such STO (001) crystals], and its value is intermediate between the ones along [001] and [1-10] in STO (110). This agrees with previous reports that in STO (001) the domains are randomly oriented (the crystal is fully twinned), whereas in STO (110) the domains are preferentially oriented (the crystal is partially detwinned) with the tetragonal axis along the [001] direction. A similar behavior has been observed for all our STO (110) crystals in their pristine state.

Next, we show in Fig. 1(d) that a fully detwinned monodomain state can be induced in STO (110) by applying a moderate uniaxial stress along the [1-10] direction. This stress gives rise to a small compression of the Ti-O bonds along [1-10] and, likewise, a small expansion along [001] and [1-10]. This provides an additional incentive for the longer c axis to be oriented along the [001] direction. For these measurements the STO (110) sample of dimensions $10 \times 10 \times 0.5$ mm^3 was mounted in a spring-loaded holder that applies a uniaxial stress of about 2.3 MPa during the cooling from room temperature

to 10 K (at a rate of 3 K/min) and the subsequent optical measurement. Figure 1(d) confirms that the R mode is now absent along the [001] direction; that is, its oscillator strength is zero within the accuracy of the measurement. The oscillator strength along the [1-10] direction exhibits a corresponding increase compared to the pristine state. The absence of the R mode for the polarization along [001] suggests that the STO (110) crystal is in a monodomain state with the tetragonal axis parallel to the [001] direction. We also found that the STO (110) crystal has a memory of this monodomain state that was almost perfectly maintained after the sample was warmed to room temperature and slowly cooled again to 10 K without the uniaxial stress. Such a memory of the monodomain state was observed for all the STO (110) samples. To erase this memory of the monodomain state, it was necessary to heat the sample to an even higher temperature of $T \geqslant 410$ K. Likewise, the twinning of the STO (110) crystal can be restored and even strongly enhanced compared to the pristine state if the stress is applied along the [001] direction. Figure 1(d) confirms that this yields nearly equal oscillator strengths for the R mode along the [001] and [1-10] directions. Note that for the STO (001) crystals we found that such a weak uniaxial pressure does not have a noticeable effect on the directional dependence of the oscillator strength of the R mode and thus on the degree of twinning.

In the following we use the possibility to obtain STO (110) crystals with a monodomain tetragonal state below $T^* = 105$ K to study the intrinsic anisotropy of the other IR-active phonon modes. For corresponding STO (001) crystals this is a difficult task that typically requires very high pressure or electric fields. Both of these requirements are hard to meet for samples that are large enough for accurate THz- and IR-spectroscopy studies. Figure 2 shows the data of the STO (110) crystal in the stressed state for the external mode at 170 cm^{-1} and the stretching mode at 545 cm^{-1} in terms of the optical conductivity measured along the [001] and [1-10] directions. In the cubic state at $T = 115$ K $> T^* = 105$ K, there is no sign of an anisotropy of these phonon modes; that is, the conductivity in the [001] and [1-10] directions agrees within the noise level [see Figs. 2(a) and 2(d)]. A small, yet clearly resolved, anisotropy appears only in the tetragonal state at $T < T^* = 105$ K, where both TO modes become slightly harder along the [001] direction and softer along [1-10]. This agrees with the expectation that the tilting of the Ti-O bonds in the plane perpendicular to the rotation axis (tetragonal axis) leads to a softening of the phonon modes (see, e.g., Ref. [34]). To quantify this anisotropy, we parameterized the phonon modes using a modified Lorentzian model, the so-called coupled-phonon model [35], which yields the following expression of the complex dielectric function:

$$\varepsilon(\omega) = \varepsilon_1(\omega) + i\varepsilon_2(\omega) = \varepsilon_\infty + \sum_{j=1}^{K} S_j \frac{\omega_j^2 - i\omega\sigma_j}{\omega_j^2 - \omega^2 - i\omega\gamma_j}.$$

(1)

This model accounts for phonon modes that are asymmetric due to disorder or anharmonicity effects, as is required for a good description of the phonon modes in STO [35,36]. It
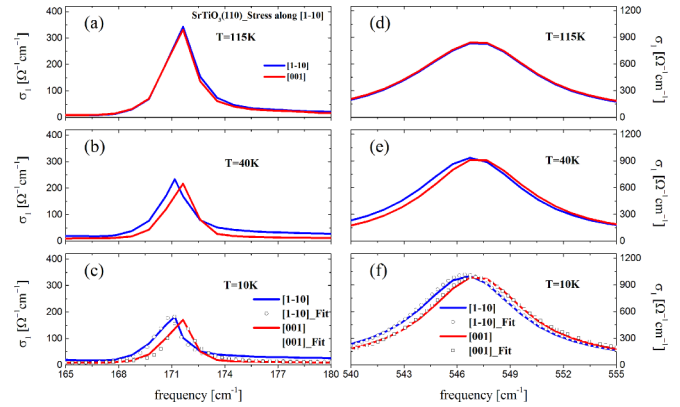

FIG. 2. Anisotropy of the phonon modes at 170 and 545 cm^{-1} along the [1-10] and [001] directions for STO (100). The crystal was cooled under a uniaxial stress of 2.3 MPa that was applied along the [1-10] direction such that it is in a monodomain state with the tetragonal axis along [001]. (a) and (d) Spectra of the optical conductivity in the cubic state at $T = 115$ K $> T^*$, for which the phonon modes are isotropic. The corresponding spectra below T^*, where the phonon modes exhibit a small, yet clearly resolved splitting, are shown at 40 K in (b) and (e) and at 10 K in (c) and (f). The splitting at 10 K is well reproduced by the fits with a so-called coupled-phonon model [35] that are shown by the open circles in (c) and (f) (the parameters are listed in Table I).

contains the usual parameters, like the broadening γ_j, the resonance frequency ω_j, and the oscillator strength S_j of the jth phonon mode. The coupling between these modes arises from the extra term $i\omega\sigma_j$ in the numerator that is subject to the condition $\sum_{j=1}^{K} S_j\sigma_j = 0$, which ensures that the Kramers-Kronig consistency is maintained [35]. The background term ε_∞ accounts for the frequency-independent contribution from the excitations at higher energies. The best fits are shown in Fig. 2 by the open symbols and describe the phonon modes rather well (except for a small and only weakly frequency dependent offset to the conductivity along [001] that most likely arises from a spurious reflection on the clamp). The obtained parameters for the eigenfrequency, the broadening, and the oscillator strengths of the phonon modes are listed in Table I. The parameters for σ_j and ε_∞ were adopted from Refs. [37,38], and the ones for the soft mode were obtained from the THz data as described below.

The weak splitting of the eigenfrequencies of the external mode at 170 cm^{-1} and the stretching mode at 545 cm^{-1} of about 1 and 0.7 cm^{-1}, respectively, are in good agreement with the small anisotropy ratio of the lattice parameters of $c/a \approx 1.0015$ [6]. Note that the contribution of the weak applied stress of 2.3 MPa to the splitting of the phonon modes is expected to be less than 0.1 cm^{-1}. This estimate is based on the pressure dependence of the Raman modes [39] as well as the pressure and temperature dependence of the lattice parameter [6,39] and the temperature dependence of the eigenfrequency of the phonon modes of STO [37].

Figure 3 shows simulations and our THz data for the corresponding anisotropy of the soft mode in STO (110). Figures 3(a) and 3(b) show the calculated values of the ellipsometric angles Ψ and Δ as obtained with an isotropic phonon model at 100 K (black line) and with an anisotropic model

TABLE I. Phonon parameters of STO (110) stressed along [1-10] obtained from the best fit to the 10 K data using the so-called coupled-phonon model of Ref. [35].

	Direction	External mode	R mode	Stretching mode
Energy (cm^{-1})	[1-10]	170.43 ± 0.06	437.8 ± 0.03	546.01 ± 0.01
	[001]	171.40 ± 0.05		546.72 ± 0.02
Oscillator strength	[1-10]	0.72 ± 0.03	0.01 ± 0.001	1.45 ± 0.03
	[001]	0.67 ± 0.03		1.37 ± 0.03
Broadening (cm^{-1})	[1-10]	1.51 ± 0.02	4.50 ± 0.02	6.99 ± 0.02
	[001]	1.51 ± 0.01		6.99 ± 0.01

below 100 K (colored lines). The phonon parameters used for these calculations were obtained from Refs. [34,36,37]. In particular, we have adopted from the Raman data in Ref. [34] the anisotropy of the TO frequency at 10 K, which amounts to $\omega_{TO} = 8$ and $17\,\mathrm{cm}^{-1}$ along [1-10] and [001], respectively. This splitting of the soft mode decreases with increasing temperature and vanishes at T^*. The spectral weight of the soft mode is assumed to be temperature independent and identical for both orientations. This assumption is consistent with the far-IR response and leads to a virtually constant value of the corresponding LO frequency, in agreement with Ref. [36] and also with our loss function spectra that are shown in Fig. 4. These spectra show that the highest LO mode is centered around 806 cm^{-1} and exhibits an anisotropy of less than 0.5 cm^{-1} between the [1-10] and [001] directions. Such a small anisotropy is expected since this LO mode contains a large contribution from the soft mode and ω_{LO} is the mean-square value of the contributions from the Coulomb repulsion and the restoring force of the Ti-O bonds, of which only the latter is affected by the lattice anisotropy.

The broadening γ was set to 6, 5, 4, 3, and 3 cm^{-1} at 100, 80, 50, 30, and 10 K, respectively, in agreement with Refs. [34,36,37]. Figures 3(a) and 3(b) show that the spectra of Ψ and Δ exhibit pronounced kinks in the vicinity of ω_{TO}
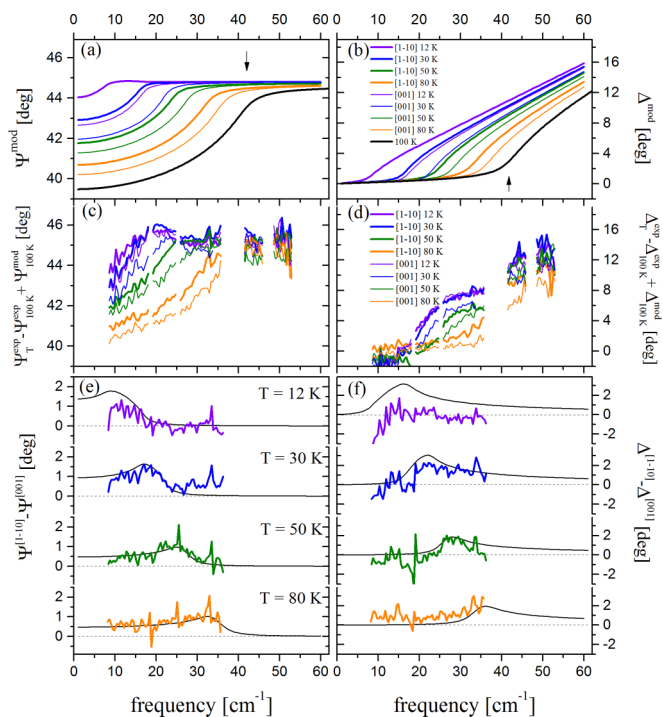

FIG. 3. Anisotropy of the soft mode of STO (110) in the THz range. (a) and (b) Calculated spectra of the ellipsometric angles Ψ and Δ for the isotropic soft mode response at 100 K and the anisotropic one at lower temperatures. The used phonon parameters are specified in the text. (c) and (d) Measured spectra of Ψ and Δ for the orientations along [1-10] and [001] (with the sample clamped along [1-10]). To remove artifacts related to light scattered on the clamp, the plots show the difference spectra with respect to 100 K to which the calculated spectrum at 100 K [thick black lines in (a) and (b)] has been added. (e) and (f) Comparison of the calculated (black line) and measured anisotropies of Ψ and Δ between the [1-10] and [001] directions.
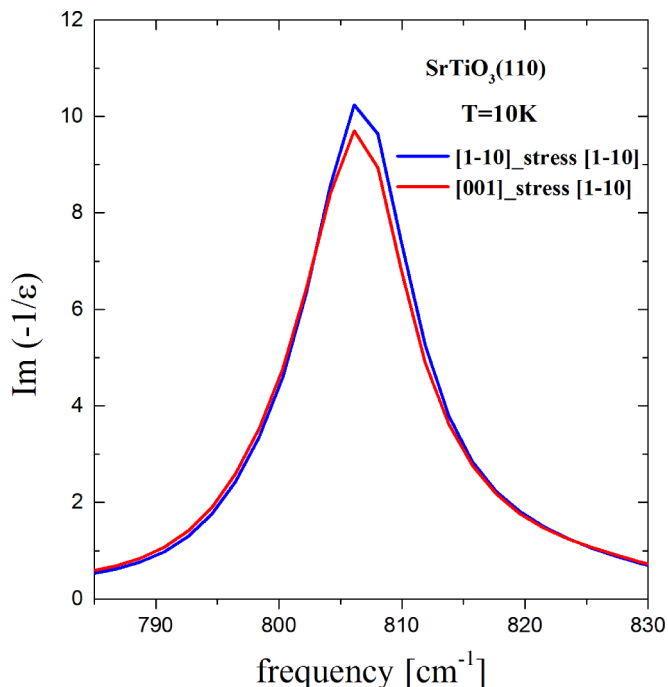

FIG. 4. Spectra of the loss function in the vicinity of the highest LO phonon mode of STO (110) in the monodomain state as obtained by cooling the sample under uniaxial stress of 2.3 MPa applied along the [1-10] direction. A very small anisotropy of the highest LO mode of less than 0.5 cm^{-1} is seen between the responses along the [001] and [1-10] directions.

that are marked by solid arrows for the spectrum at 100 K, for which $\omega_{TO} = 41.8\ \text{cm}^{-1}$.

The experimental spectra of Ψ and Δ in the THz regime are strongly affected by stray light that is reflected from the clamp in which the sample is mounted (due to the rather large focal spot of the THz beam) and also by diffraction effects. They are shown in the Appendix together with the difference plots with respect to the data at 100 K. In Figs. 3(c) and 3(d), in an attempt to suppress these experimental artifacts, we present the data in terms of the difference spectra of Ψ and Δ with respect to the curves at 100 K to which the calculated spectrum at 100 K [solid lines in Fig. 3(a) and 3(b)] has been added. These spectra provide evidence for a sizable anisotropy of the soft mode below 100 K. The comparison between the calculated (black lines) and the measured anisotropy of Ψ and Δ between the [1-10] and [001] directions is shown in Figs. 3(e) and 3(f). The fair agreement between the calculated and the measured data (except for a frequency-independent vertical offset of some spectra that is likely due to an incomplete suppression of the stray light signal) confirms that the soft mode develops a sizable anisotropy below T^*.

Finally, we discuss an additional sharp feature around 480 cm^{-1} in the IR spectra of STO (110) that becomes very pronounced in the monodomain state at low temperature. Figure 5 shows the spectra of the ellipsometric angle Ψ of STO (110) in the frequency range between 425 and 500 cm^{-1}, which includes the R mode at 438 cm^{-1}, from which the degree of twinnin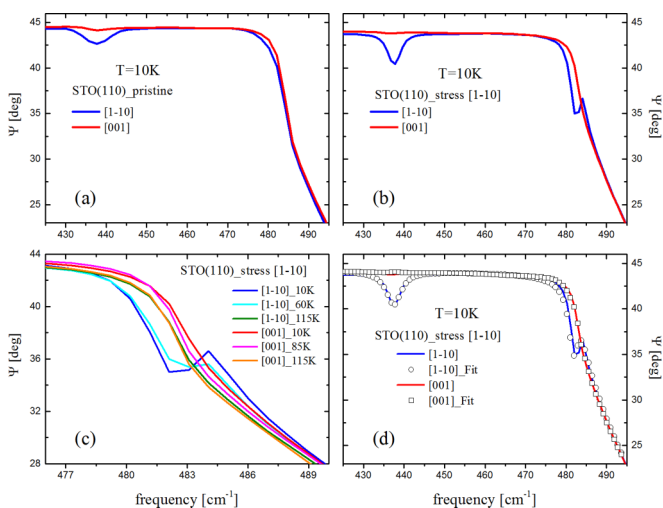g can be deduced. The new feature develops around 480 cm^{-1}, very close to a longitudinal optical phonon mode frequency at which the real part of the dielectric function ε_1 crosses zero. Figures 5(a) and 5(b) compare the spectra for the partially twinned pristine and monodomain states. In the monodomain state, there is a rather sharp dip feature in the spectrum along [1-10] that is absent along [001]. In the pristine state this dip feature is much broader and therefore barely visible as a small difference between the spectra along [1-10] and [001]. Figure 5(c) shows that this dip feature at 480 cm^{-1} in the monodomain state along [1-10] vanishes when the temperature is increased above the structural transition at $T^* = 105$ K, where the spectra for [1-10] and [001] agree within the noise level.

In the following we show that this dip feature can be understood in terms of the anisotropy of the IR-active phonon modes. Specifically, it results from a small splitting of the zero crossings of ε_1 along the [1-10] and [001] directions that is mainly caused by the splitting of the soft mode along the in-plane directions. Figure 5(d) shows that this feature can be reproduced with a modified version of the coupled-phonon model [35] which takes into account the anisotropy of the phonon modes along the [001] and the [1-10] directions. For the simulation shown by the open symbols in Fig. 5(d) we used for the phonon modes at 170, 438, and 545 cm^{-1} the eigenfrequency, oscillator strength, and broadening as listed in Table I and the corresponding phonon asymmetries and value of ε_∞ as reported in Refs. [37,38]. For the soft mode we used a splitting of the TO mode that is somewhat smaller than the one reported in Ref. [34] and used in describing the THz data in Fig. 3. The eigenfrequency of the highest LO mode of $\omega_{LO} = 806\ \text{cm}^{-1}$ has been obtained from the data in Fig. 4.

An alternative interpretation of this dip feature around 480 cm^{-1} in terms of a plasmonic effect due to a so-called Berreman mode [40], which arises from mobile charge carriers that are confined to the surface of the sample, can be discarded. Such a Berreman mode was observed at the interface of LAO/STO heterostructures, where it gives rise to a pronounced dip feature at the highest LO phonon mode of STO around 865 cm^{-1} [41,42]. Nevertheless, the present STO (110) sample does not have such a heterointerface, and furthermore, a corresponding dip feature does not occur at the highest LO edge near 865 cm^{-1}, where, according to the Berreman-mode scenario, it should be strongest.

IV. SUMMARY

In summary, with IR and THz ellipsometry we have studied the IR-active phonon modes of SrTiO$_3$ (110) crystals. In particular, we have shown that the anisotropy of the oscillator strength of the so-called R mode at 438 cm^{-1}, which becomes IR active below the antiferrodistortive cubic-to-tetragonal phase transition at $T* = 105$ K, can be used to determine the degree of twinning of these STO (110) crystals. Notably, we found that a weak stress of about 2.3 MPa along the [1-10] direction, which can be readily applied with a spring-loaded clamp, is sufficient to induce a monodomain state with the tetragonal axis along the [001] direction. Likewise, a polydomain state can be (re)established if the stress is applied along [001]. We have used this possibility to control the domain state in STO (110) to study the weak intrinsic anisotropy of the eigenfrequency of the IR-active phonon modes below T^*.

FIG. 5. Dip feature in the spectrum of Ψ in the vicinity of the LO mode of STO (110) around 480 cm^{-1} and its dependence on the structural domain state. Also shown is the R mode around 438 cm^{-1} from which the degree of detwinning can be deduced. (a) and (b) Data for STO (110) in a pristine state and after cooling under uniaxial stress along [1-10] where the crystal is still partially twinned and in a monodomain state, respectively. The comparison of the spectra in (a) and (b) shows that the dip feature around 480 cm^{-1} is more pronounced and sharper in the monodomain state. (c) Evolution of the dip feature in the monodomain state as a function of temperature. (d) Comparison of the experimental data in the monodomain state at 10 K (solid lines) with the fit using an anisotropic version of the coupled-phonon model (open circles).

In the future this could be a useful tool to study, for example, the influence of the domain boundaries on the charge-carrier dynamics in doped samples or the electronic and magnetic properties of the various kinds of thin films and multilayers that can be grown on top of such STO (110) single crystals.

ACKNOWLEDGMENTS

APPENDIX: THZ SPECTRA

Figures 6 and 7 show the as-measured spectra of Ψ and Δ in the THz range as obtained with the time-domain THz ellipsometer along the [1-10] and [001] directions, respectively. The insets of Figs. 6(a) and 7(a) sketch how the sample was mounted in a clamp to apply the uniaxial stress along the [1-10] direction and also the optical reflection geometry. Due to the long wavelength of the THz radiation, diffraction effects [43] start to play a significant role. In addition, the focal spot size, even on the diffraction limit, becomes comparable to the size of the sample. In this respect, the light that is reflected or diffracted from the clamp will also strongly affect the THz
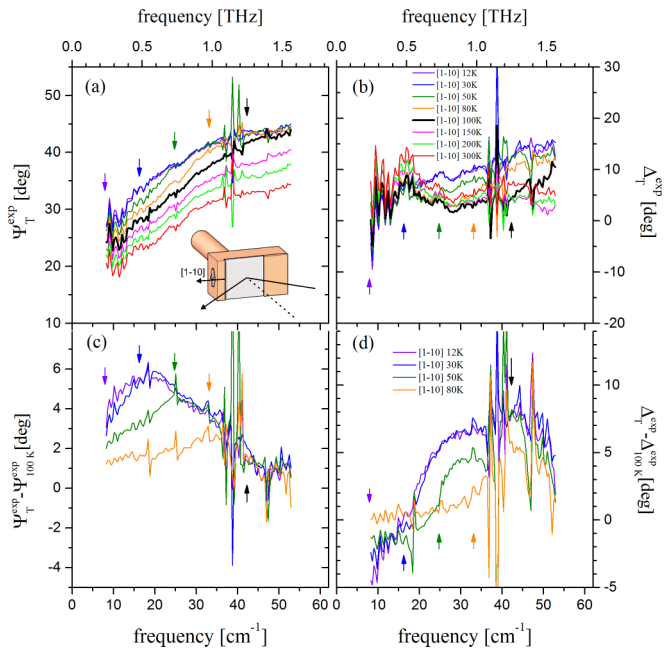

FIG. 7. (a) and (b) As-measured THz spectra of the ellipsometric angles, Ψ^{exp} and Δ^{exp}, at different temperatures for the plane of incidence of the light along the [001] direction. The inset in (a) shows how the STO (110) crystal was mounted in a spring-loaded clamp to apply a weak stress along the [1-10] direction to induce a monodomain state below $T^* = 105$ K. The arrows indicate the position of the soft mode at the different temperatures. (c) and (d) Temperature difference spectra with respect to 100 K, $\Psi_T^{\text{exp}} - \Psi_{100K}^{\text{exp}}$ and $\Delta_T^{\text{exp}} - \Delta_{100K}^{\text{exp}}$, of the curves shown in (a) and (b), respectively, for which the features due to the soft mode are more clearly seen. These difference spectra have been used in Figs. 3(c)–3(f).
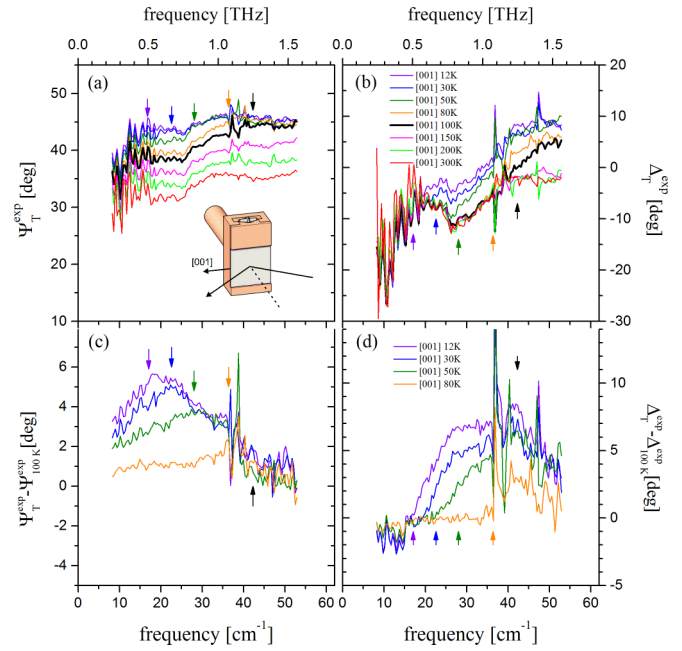

FIG. 6. (a) and (b) As-measured THz spectra of the ellipsometric angles, Ψ^{exp} and Δ^{exp}, at different temperatures with the plane of incidence of the light along the [1-10] direction. The inset in (a) shows how the STO (110) crystal was mounted in a spring-loaded clamp to apply a weak stress along the [1-10] direction to obtain a monodomain state below $T^* = 105$ K. The arrows indicate the position of the soft mode at the different temperatures. (c) and (d) Temperature difference spectra with respect to 100 K, $\Psi_T^{\text{exp}} - \Psi_{100K}^{\text{exp}}$ and $\Delta_T^{\text{exp}} - \Delta_{100K}^{\text{exp}}$, of the curves shown in (a) and (b), respectively, for which the features due to the soft mode are more clearly seen. These difference spectra have been used in Figs. 3(c)–3(f).

spectra and yield a background signal that is different for the two measurement geometries. Nevertheless, as marked by the colored arrows, the temperature dependence of the soft mode position is already apparent in the raw ellipsometric spectra in Figs. 6(a) and 6(b) and 7(a) and 7(b).

Figures 6(c) and 6(d) and 7(c) and 7(d) display the corresponding temperature difference plots with respect to the experimental data at 100 K. This helps to suppress the spurious background and enhance the relevant information about the temperature dependence and the anisotropy of the soft mode. The colored arrows mark once more the characteristic features due to the soft mode which are discernible, especially in the spectra of $\Psi_T^{\text{exp}} - \Psi_{100K}^{\text{exp}}$. Note that the subtracted 100 K spectrum manifests as a kink in $\Psi_T^{\text{exp}} - \Psi_{100K}^{\text{exp}}$ and in $\Delta_T^{\text{exp}} - \Delta_{100K}^{\text{exp}}$ around 42 cm^{-1}, as marked by a black arrow. For the curves shown in Figs. 3(c) and 3(d) we have added to the experimental temperature difference spectra in Figs. 6(c) and 6(d) and 7(c) and 7(d) a model spectrum for Ψ and Δ at 100 K (that is isotropic). This was done for the reader's convenience to further reduce the influence of the diffraction effect and the spurious signal from the sample holder. Furthermore, to visualize the anisotropy of the spectra for the two orientations, we have plotted their mutual difference in Figs. 3(e) and 3(f). The latter is independent of the previously added isotropic 100 K model line.

[1] A. Ohtomo and H. Y. Hwang, Nature (London) **427**, 423 (2004).

[2] S. Thiel, G. Hammerl, A. Schmehl, C. W. Schneider, and J. Mannhart, Science **313**, 1942 (2006).

[3] N. Reyren, S. Thiel, A. D. Caviglia, L. F. Kourkoutis, G. Hammerl, C. Richter, C. W. Schneider, T. Kopp, A.-S. Rüetschi, D. Jaccard, M. Gabay, D. A. Muller, J.-M. Triscone, and J. Mannhart, Science **317**, 1196 (2007).

[4] C. Bell, S. Harashima, Y. Kozuka, M. Kim, B. G. Kim, Y. Hikita, and H. Y. Hwang, Phys. Rev. Lett. **103**, 226802 (2009).

[5] J. A. Sulpizio, S. Ilani, P. Irvin, and J. Levy, Annu. Rev. Mater. Res. **44**, 117 (2014).

[6] R. Loetzsch, A. Lübcke, I. Uschmann, E. Förster, V. Große, M. Thuerk, T. Koettig, F. Schmidl, and P. Seidel, Appl. Phys. Lett. **96**, 071901 (2010).

[7] F. W. Lytle, J. Appl. Phys. **35**, 2212 (1964).

[8] W. Zhong and D. Vanderbilt, Phys. Rev. B **53**, 5047 (1996).

[9] K. A. Müller and H. Burkard, Phys. Rev. B **19**, 3593 (1979).

[10] D. E. Grupp and A. M. Goldman, Science **276**, 392 (1997).

[11] P. A. Fleury, J. F. Scott, and J. M. Worlock, Phys. Rev. Lett. **21**, 16 (1968).

[12] E. Sawaguchi, A. Kikuchi, and Y. Kodera, J. Phys. Soc. Jpn. **18**, 459 (1963).

[13] J. Hoppler, J. Stahn, H. Bouyanfif, V. K. Malik, B. D. Patterson, P. R. Willmott, G. Cristiani, H.-U. Habermeier, and C. Bernhard, Phys. Rev. B **78**, 134111 (2008).

[14] B. Kalisky, E. M. Spanton, H. Noad, J. R. Kirtley, K. C. Nowack, C. Bell, H. K. Sato, M. Hosoda, Y. Xie, Y. Hikita, C. Woltmann, G. Pfanzelt, R. Jany, C. Richter, H. Y. Hwang, J. Mannhart, and K. A. Moler, Nat. Mater. **12**, 1091 (2013).

[15] M. Honig, J. A. Sulpizio, J. Drori, A. Joshua, E. Zeldov, and S. Ilani, Nat. Mater. **12**, 1112 (2013).

[16] T. S. Chang, J. Appl. Phys. **43**, 3591 (1972).

[17] K. A. Müller, W. Berlinger, M. Capizzi, and H. Gränicher, Solid State Commun. **8**, 549 (1970).

[18] D. van Mechelen, Ph.D. thesis, University of Geneva, 2010.

[19] T. S. Chang, J. F. Holzrichter, G. F. Imbusch, and A. L. Schawlow, Appl. Phys. Lett. **17**, 254 (1970).

[20] Z. Wang, Z. Zhong, X. Hao, S. Gerhold, B. Stöger, M. Schmid, J. Sánchez-Barriga, A. Varykhalov, C. Franchini, K. Held, and U. Diebold, Proc. Natl. Acad. Sci. USA **111**, 3933 (2014).

[21] A. Annadi, Q. Zhang, X. R. Wang, N. Tuzla, K. Gopinadhan, W. M. Lü, A. Roy Barman, Z. Q. Liu, A. Srivastava, S. Saha, Y. L. Zhao, S. W. Zeng, S. Dhar, E. Olsson, B. Gu, S. Yunoki, S. Maekawa, H. Hilgenkamp, T. Venkatesan, and Ariando, Nat. Commun. **4**, 1838 (2013).

[22] F. Bottin, F. Finocchi, and C. Noguera, Surf. Sci. **574**, 65 (2005).

[23] R. I. Eglitis and D. Vanderbilt, Phys. Rev. B **77**, 195408 (2008).

[24] J. A. Enterkin, A. K. Subramanian, B. C. Russell, M. R. Castell, K. R. Poeppelmeier, and L. D. Marks, Nat. Mater. **9**, 245 (2010).

[25] J. Chrosch and E. K. H. Salje, J. Phys. Condens. Matter **10**, 2817 (1998).

[26] C. Bernhard, J. Humlíček, and B. Keimer, Thin Solid Films **455**, 143 (2004).

[27] P. Marsik, K. Sen, J. Khmaladze, M. Yazdi-Rizi, B. P. P. Mallett, and C. Bernhard, Appl. Phys. Lett. **108**, 052901 (2016).

[28] D. E. Aspnes, J. Opt. Soc. Am. **70**, 1275 (1980).

[29] Y. Kozuka, Y. Hikita, T. Susaki, and H. Y. Hwang, Phys. Rev. B **76**, 085129 (2007).

[30] J. Hlinka, J. Petzelt, S. Kamba, D. Noujni, and T. Ostapchuk, Phase Transitions **79**, 41 (2006).

[31] T. Trautmann and C. Falter, J. Phys. Condens. Matter **16**, 5955 (2004).

[32] J. Petzelt, T. Ostapchuk, I. Gregora, I. Rychetský, S. Hoffmann-Eifert, A. V. Pronin, Y. Yuzyuk, B. P. Gorshunov, S. Kamba, V. Bovtun, J. Pokorný, M. Savinov, V. Porokhonskyy, D. Rafaja, P. Vaněk, A. Almeida, M. R. Chaves, A. A. Volkov, M. Dressel, and R. Waser, Phys. Rev. B **64**, 184111 (2001).

[33] M. Rössle, K. W. Kim, A. Dubroka, P. Marsik, C. N. Wang, R. Jany, C. Richter, J. Mannhart, C. W. Schneider, A. Frano, P. Wochner, Y. Lu, B. Keimer, D. K. Shukla, J. Strempfer, and C. Bernhard, Phys. Rev. Lett. **110**, 136805 (2013).

[34] A. Yamanaka, M. Kataoka, Y. Inaba, K. Inoue, B. Hehlen, and E. Courtens, Europhys. Lett. **50**, 688 (2000).

[35] J. Humlíček, R. Henn, and M. Cardona, Phys. Rev. B **61**, 14554 (2000).

[36] I. Fedorov, V. Železný, J. Petzelt, V. Trepakov, M. Jelínek, V. Trtík, M. Čerňanský, and V. Studnička, Ferroelectrics **208**, 413 (1998).

[37] M. Rössle, Ph.D. thesis, University of Fribourg, 2013.

[38] M. Rössle, C. N. Wang, P. Marsik, M. Yazdi-Rizi, K. W. Kim, A. Dubroka, I. Marozau, C. W. Schneider, J. Humlíček, D. Baeriswyl, and C. Bernhard, Phys. Rev. B **88**, 104110 (2013).

[39] M. Guennou, P. Bouvier, J. Kreisel, and D. Machon, Phys. Rev. B **81**, 054115 (2010).

[40] D. W. Berreman, Phys. Rev. **130**, 2193 (1963).

[41] A. Dubroka, M. Rössle, K. W. Kim, V. K. Malik, L. Schultz, S. Thiel, C. W. Schneider, J. Mannhart, G. Herranz, O. Copie, M. Bibes, A. Barthélémy, and C. Bernhard, Phys. Rev. Lett. **104**, 156807 (2010).

[42] M. Yazdi-Rizi, P. Marsik, B. P. P. Mallett, A. Dubroka, D. V. Christensen, Y. Z. Chen, N. Pryds, and C. Bernhard, Europhys. Lett. **113**, 47005 (2016).

[43] J. Humlíček and C. Bernhard, Thin Solid Films **455**, 177 (2004).